

Insight into the mechanisms of columnar to equiaxed grain transition during metallic additive manufacturing

Pengwei Liu^{a,b}, Zhuo Wang^b, Yaohong Xiao^b, Mark F. Horstemeyer^b, Xiangyang Cui^{a,*}, Lei Chen^{b,*}

^a State Key Laboratory of Advanced Design and Manufacturing for Vehicle Body, Hunan University, Changsha, 410082, PR China

^b Department of Mechanical Engineering, Mississippi State University, MS, 39762, USA

ARTICLE INFO

Keywords:

Columnar to equiaxed transition
Constitutional supercooling
Heterogeneous nucleation
Additive manufacturing
Multiscale phase-field model

ABSTRACT

The columnar to equiaxed transition (CET) of grain structures associated with processing conditions has been observed during metallic additive manufacturing (AM). However, the formation mechanisms of these grain structures have not been well understood under rapid solidification conditions, especially for AM of superalloys. This paper aims to uncover the underlying mechanisms that govern the CET of AM metals, using a well-tested multiscale phase-field model where heterogeneous nucleation, grain selection and grain epitaxial growth are considered. Using In718 as an example, the simulated results show that the CET is critically controlled by the undercooling, involving constitutional supercooling, thermal and curvature undercoolings in the melt pool, which dictates the extent of heterogeneous nucleation with respect to the grain epitaxial growth during rapid solidification.

1. Introduction

The control of grain structures and textures during metallic additive manufacturing (AM), e.g., nickel-based superalloys [1–4], is critical for acquiring desirable mechanical properties. However, high energy input of selective laser melting (SLM) or electron beam melting (EBM) introduces a steep thermal gradient near the melt pool in favor of the development of columnar grains and thus deteriorating the mechanical properties of AM metallic builds.

Enormous experimental efforts [5–9] have thus been stimulated to develop various strategies to refine the columnar grains to the equiaxed grains, i.e., columnar to equiaxed transition (CET), to achieve favorable mechanical properties. Price, Cheng, Chou et al. [10,11] have studied the effects of process parameters and scanning strategies on the microstructures and mechanical properties during AM of Ti-6Al-4V alloy. Dinda et al. [2] have demonstrated that the microstructure can be controlled by varying the laser scanning patterns during laser deposition of nickel-based superalloys. Unidirectional laser scanning pattern preferred a fiber texture, while bidirectional laser scanning patterns produced the rotated cube texture. More detailed investigations about the texture-controlled of direct laser fabricated IN718 have been studied by Parimi et al. [12]. They found that, at the lower laser powers, both unidirectional and bidirectional scanning patterns developed the

banded grain structures including the inclined columnar grains and fine equiaxed grains in one layer (see Fig. 3b). However, very large columnar grains were generated along the building direction at higher laser powers. To achieve the CET of grain structures, Raghavan and Babu et al. [13,14] have proposed a spot melting scan strategy for the EBM of nickel-based superalloys, which successfully manipulated the grain structures and crystallographic textures of the printed components. However, direct observations of grain structure evolutions were quite difficult due to the rapid solidification during metallic AM. The fundamental understanding about the formation mechanisms of CET of grain structures essentially associated with the undercooling, ΔT , thermal gradient, G , and solidification rate, R , requires further research.

In recent years, the numerical simulation technique has made spectacular progress as a powerful tool to help understand the metal-based AM process. For example, Loh et al. [15] have studied the SLM process by using a finite element model (FEM), with the focus on powder to solid transition, volume shrinkage and material removal. These physical phenomena made significant influence on temperature field development. Foroozmehr et al. [16] have predicted the temperature distributions and melt pool dimensions in a multi-tracks pattern during one layer printing using a finite element simulation. They found that the melt pool dimensions achieved the steady conditions after the third track, and the melt pool depth stayed almost constant of

* Corresponding authors.

E-mail addresses: cuixy@hnu.edu.cn (X. Cui), chen@me.msstate.edu (L. Chen).

<https://doi.org/10.1016/j.addma.2018.12.019>

Received 3 July 2018; Received in revised form 17 November 2018; Accepted 22 December 2018

Available online 24 December 2018

2214-8604/ © 2019 Elsevier B.V. All rights reserved.

2 mm. Our group [17] have also investigated the thermal responses of selective electron beam melting (SEBM) of Ti-6Al-4V alloy using a “Tri-Prism” finite element method [18–20]. The temperature distributions, temperature cycles and thermal gradient histories during the single layer and multi-layer building process have been studied in detail. In order to simulate the evolution of microstructure, a phase-field model has been developed by Krill and Chen et al. [21,22] without explicitly tracking of interface positions. It has been used for the analyses of dendrite growth, including selective laser melting [23], welding [24] and lithium battery [25–28], phase transformation [29,30], isothermal grain growth [21,31] and recrystallization [32]. To further extend the application field, we have developed a multiscale model [33] by integrating the finite element method and the phase-field model for the simulation of grain growth during SEBM of Ti-6Al-4V. In this study, it was found that peak temperature and steep thermal gradient were formed near the melt pool, resulting in the development of large columnar and slanted inward grain structures. This ultimately led to the anisotropic mechanical properties of as-built components. To alleviate the mechanical anisotropy, we further studied the CET mechanisms of grain structures during metallic additive manufacturing.

In this work, the CET mechanisms of grain structures are investigated by using a well-tested multiscale phase-field model (PFM) [33] where heterogeneous nucleation, grain selection and grain epitaxial growth are considered during metallic AM. Two different scanning strategies with various processing variables, performed in the experiments [12,13], are used to generate a series of shapes of melt pool with various solute and temperature distributions. The undercooling, involving constitutional supercooling, thermal and curvature undercoolings in the melt pool, is then correlated with the simulated grain structures. Comprehensive analyses of these correlations uncover the underlying mechanisms that govern the CET of AM metals.

2. Numerical model

Three dimensional numerical simulations, including heat and mass transfer, as well as solidified grain growth in the melt pool, are performed using a modified multiscale model based on our previous study [32–34]. Specifically, the thermal responses at the macroscale are predicted using the finite-element method, and the thermal information extracted from thermal model is then input into the PFM to simulate the grain development at the mesoscale.

As illustrated in Fig. 1a, the solidified grain growth can be either in an epitaxial manner or resulted from the heterogeneous nucleation [35,36]. The grain heterogeneous nucleation owing to the solute segregation is newly incorporated in the present model, in addition to the grain epitaxial growth involved in the published model [33]. The dominance of each way essentially depends on the spatially localized

solute and temperature fields in the melt pool, see Fig. 1b and c. As the solute diffuses near the solid/liquid (S/L) interface, there is a decrease of liquidus temperature, T_L , of the alloy, due to the solute accumulation, C_L^* , at the front of grains that deviates from the reference solute concentration, C_0 , *i.e.*, the solute concentration of nominal alloy composition in the liquid. As a result, the constitutional supercooling, ΔT_c , defined as the difference between the liquidus temperature, T_L , and the actual temperature, T_{actual} occurs in the mushy zone divided by the liquidus (L) and solidus (S). Further considering the thermal undercooling, ΔT_t , generated as the solidification latent heat, and the curvature undercooling, ΔT_r , as usual, the total undercooling ΔT can be expressed as follows [37]

$$\Delta T = \Delta T_c + \Delta T_t + \Delta T_r = mC_0(k-1) \left[\frac{I_v(P_c)}{1 - (1-k)I_v(P_c)} \right] + \frac{\Delta h_v}{c_p} I_v(P_t) + \frac{2\Gamma}{r}, \quad (1)$$

where m represents the liquidus slope, k is the solid/liquid partition coefficient, Δh_v is the fusion enthalpy per unit volume, c_p is the specific heat, Γ represents the Gibbs-Thomson coefficient, the Ivantsov function $I_v(P) = P \exp(P) E(P)$, and the $E(P) = \int_P^\infty \exp(-t)/t dt$, P_c and P_t are the solutal and thermal Peclet numbers, respectively

$$P_c = \frac{rR}{2D}, \quad (2a)$$

$$P_t = \frac{rR}{2h}, \quad (2b)$$

where D is the solute diffusion coefficient in the liquid, h represents the thermal diffusivity of the melt, and r is the dendrite tip radius.

For rapid solidification process, such as selective laser melting and electron beam melting, corresponding to a high Peclet number, the dendrite tip radius can be calculated by the following equation [38]

$$r = \left[\frac{\Gamma/\sigma^*}{mG_c^* - G} \right]^{1/2}, \quad (3)$$

where $\sigma^* = 1/4\pi^2$ is the marginal stability constant, and G_c^* is the effective concentration gradient. The solute concentration at the front of grains, *i.e.*, solidus phase line, is computed by

$$C_L^* = \frac{C_0}{1 - (1-k)I_v(P_c)}, \quad (4)$$

and the width of the mushy zone can be estimated from [39]

$$\delta_c = \frac{\Delta T}{G}. \quad (5)$$

It is note that G is the thermal gradient at each lattice site which varies from the top to bottom of the melt pool. The solute

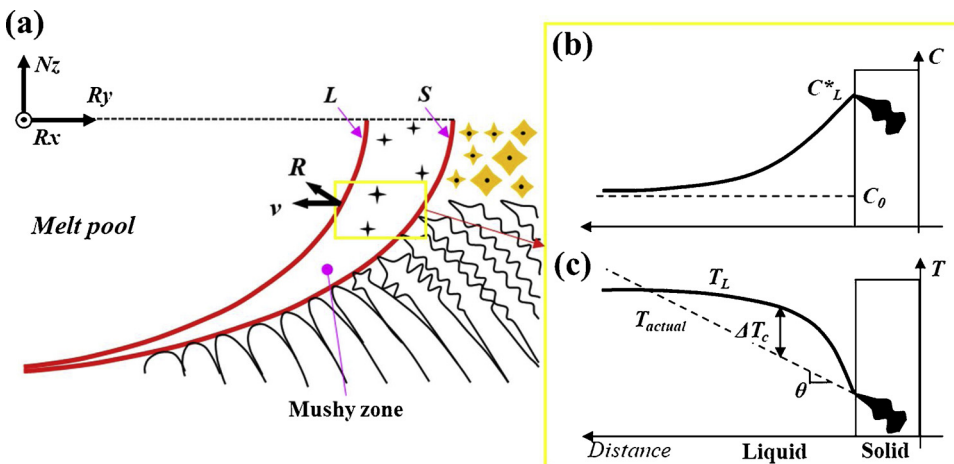


Fig. 1. (a) Schematic of grain nucleation and growth near the melt pool. L and S are liquidus and solidus, respectively. The mushy zone consists of both liquid and solid phases, (b) and (c) show the hypothetical solute concentration and corresponding temperature profiles near the solid/liquid interface. The horizontal axis represents the distance from the front of grains along solidification direction. θ is the slope of the line of actual temperature, *i.e.*, the thermal gradient.

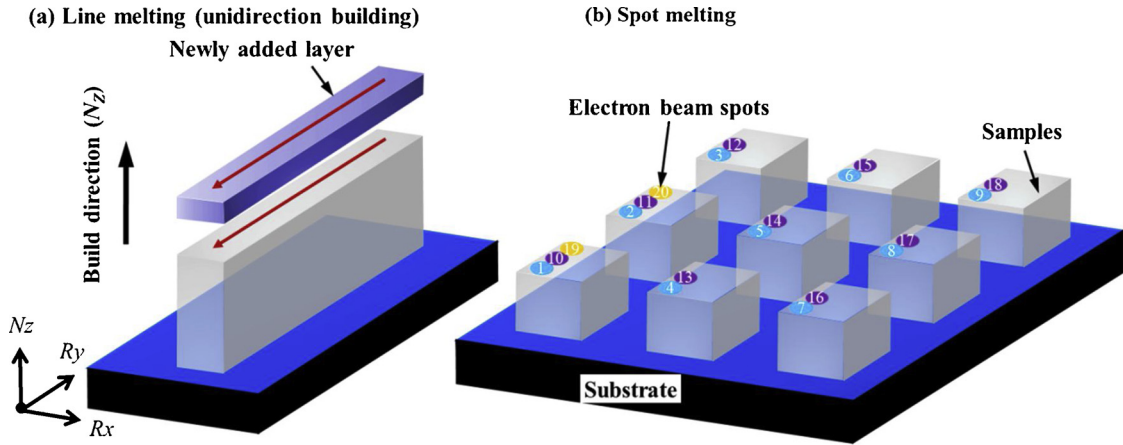


Fig. 2. (a) Unidirectional line melting strategy for selective laser melting of In718 [12], (b) spot melting strategy for electron beam melting of In718 [13].

concentration, C_L , in mushy zone can be approximated as follows

$$C_L = C_L^* - \frac{w}{\delta_c} (C_L^* - C_0), \quad 0 \leq w \leq \delta_c, \quad (6)$$

in which, w represents the distance from the solidus phase line along the direction of solidification.

In general, the heterogeneous nucleation is nearly instantaneous and depends on the undercooling, especially for constitutional supercooling for rapid solidification [40–42]. A Gaussian distribution [43] is used to characterize the density of heterogeneous nucleation as a function of undercooling

$$n(\Delta T) = \int_0^{\Delta T} \frac{dn}{dT'} d\Delta T' = \int_0^{\Delta T} \frac{n_{max}}{\Delta T_\sigma \sqrt{2\pi}} \exp\left[-\frac{1}{2} \left(\frac{\Delta T' - \Delta T_N}{\Delta T_\sigma}\right)^2\right] d\Delta T', \quad (7)$$

where ΔT_N and ΔT_σ are the mean undercooling and standard deviation of undercooling, respectively, n_{max} is the maximum density of nucleation sites. In this work, the n_{max} is $9.0 \times 10^9 \text{ m}^{-3}$, the ΔT_N is 33.6 K, the ΔT_σ is 5.0 K [44,45] for In718 alloy.

Considering the nucleation distribution described in Eq. (7), the density of new grains δn_v , formed in each time step is given by $\{n[\Delta T(t)] - n[\Delta T(t - \Delta t)]\}$. Therefore, the probability of nucleation at each lattice site can be written as

$$P_v = \delta n_v V_{ea} = \{n[\Delta T(t)] - n[\Delta T(t - \Delta t)]\} dx^3, \quad (8)$$

where $V_{ea} = dx^3$ is the effective volume of each lattice site. A random number, r_a , within [0, 1] is generated by the computer at lattice sites within the liquid region in each time step, and a new nucleus is formed at the lattice site where $r_a \leq P_v$. Otherwise, nothing happens.

3. Two scanning strategies for experimental and numerical investigations

To explore the effect of the heterogeneous nucleation on the CET of grain structures during metallic AM, two scanning strategies, including line [12] and spot [13] melting, are developed to achieve the CET of grain structures. As demonstrated by Parimi et al. [12], a laser unidirectional line melting strategy, as shown in Fig. 2a, with laser power 390 W, laser scanning speed $400 \text{ mm}\cdot\text{s}^{-1}$, and powder flow rate of 18 g min^{-1} is used to obtain the CET of grain structures. In this strategy, the laser is switched off between the layers for a time that is equal to the one of a layer deposition ($\sim 6 \text{ s}$). As the purpose of the investigation is to capture the characteristic of CET of grain structures in the melt pool, one-layer printing is simulated for the line melting strategy. The grain growth pattern of multi-layer printing strategy and the relationship between two layers had been discussed in our previous work [33].

Another strategy, a spot melting strategy, is first proposed by

Raghavan et al. [13], which can also acquire the CET or fully equiaxed grain structures during metallic AM process. Fig. 2b depicts the spot melting strategy that is used to manufacture the samples. In the spot melting, the electron beam with beam voltage of 60 kV, current of $5 \sim 20 \text{ mA}$ is turned on at a point for a period of time (spot ON time) of 0.1 or 1.0 ms. Once the time period exceeds the spot ON time, the electron beam jumps to the next spot according to the sequence described in Fig. 2b. In order to clearly characterize the grain transition structures and reduce computational cost, the process of melting and cooling of single spot is simulated for the spot melting pattern.

The current model should be applicable to predict the CET of grain structures for different materials, such as nickel-based and titanium-based alloys, as long as the corresponding material parameters are known. In this study, the In718 alloy is taken as deposited material for both the experimental and numerical investigations. The physical parameters used in the simulations are listed in Table 1.

4. Results and discussion

4.1. Grain morphologies and evolution mechanisms of CET

Fig. 3 shows the simulated and experimental [12] results of the unidirectional line melting pattern with the scanning speed of $400 \text{ mm}\cdot\text{s}^{-1}$. Fig. 3a shows the grain morphologies in the melt pool during In718 AM. It can be seen that the columnar grains grow epitaxially from the pre-deposited layer. However, the equiaxed grains formed near the centerline of the melt pool gradually suppress these columnar grains, thus giving rise to the CET of grain structures that is consistent with the experimentally observed grain structures, see Fig. 3b. Such a CET of grain structures is mainly attributed to the heterogeneous nucleation at the tail of the melt pool, as demonstrated in Fig. 3c, where the constitutional supercooling occurs due to the difference of liquidus temperature induced by the variational solute

Table 1
Physical parameters of the In718 alloy [13,37,46].

Property (units)	Symbol	Value
Liquidus temperature (K)	T_L	1610.0
Solidus temperature (K)		1528.0
Specific heat ($\text{J}\cdot\text{K}^{-1}\cdot\text{mol}^{-1}$)	c_p	42.42
Liquidus slope ($\text{K}\cdot(\text{at}\%)^{-1}$)	m	-3.50
Partition coefficient	k	0.12
Solute concentration of Ni in liquid (wt%)	C_0	52.54
Thermal diffusivity ($\text{m}^2\cdot\text{s}^{-1}$)	h	6.0×10^{-6}
Solute diffusion coefficient ($\text{m}^2\cdot\text{s}^{-1}$)	D	3.0×10^{-9}
Enthalpy of fusion ($\text{J}\cdot\text{mol}^{-1}$)	Δh_v	1.77×10^4
Gibbs-Thomson coefficient ($\text{K}\cdot\text{m}$)	Γ	1.4×10^{-7}

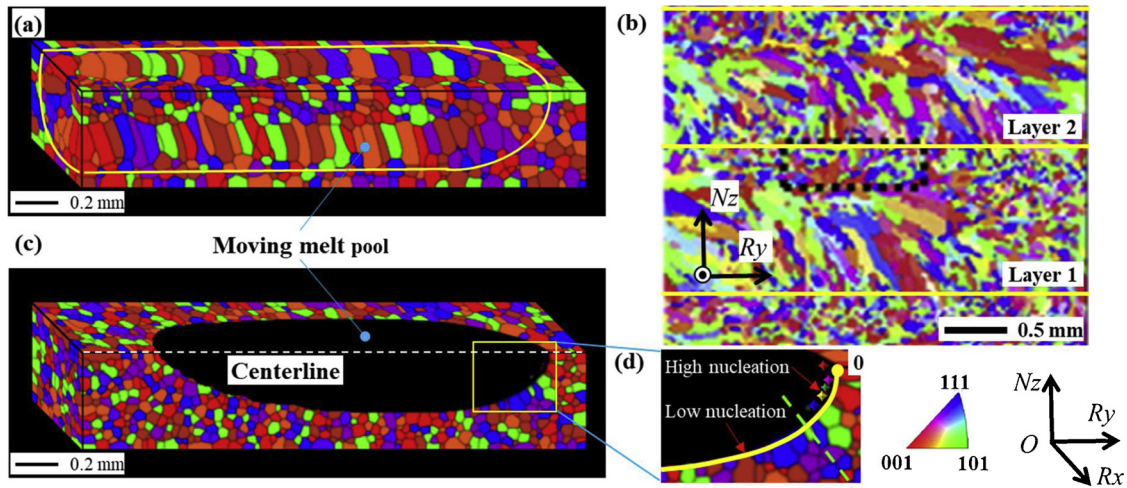


Fig. 3. Results of the unidirectional line melting strategy, (a) and (b) numerical and experimental [12] grain morphologies in the melt pool, (c) nucleation at the tail of the melt pool, and (d) schematic of the low and high nucleation zones. The yellow line shows the arc length from the top to bottom of the melt pool. (For interpretation of the references to colour in this figure legend, the reader is referred to the web version of this article).

concentration and actual temperature.

The quantitative analyses of the heterogeneous nucleation are plotted in Fig. 4, in which the arc length represents the distance from the top to bottom of the melt pool along liquidus in the longitudinal section $\angle N_z O R_y$ (see the yellow curve in Fig. 3d). The mean undercooling is set as $\Delta T_N = 33.6$ K [44] and the standard deviation as $\Delta T_\sigma = 5.0$ K [45] for In718 AM. An important finding is that the undercooling is relatively small ($\Delta T < 1.0$ K) at the bottom of the melt

pool. Therefore, it is not adequate to trigger the heterogeneous nucleation physically, and the grain growth occurs in an epitaxial manner. Accordingly, the probability of the heterogeneous nucleation is considerably low as illustrated in the inset in Fig. 4a. The undercooling, contributed mostly by the constitutional supercooling, is remarkably increased when approaching the top or near the tail of the melt pool. Specifically, when the distance to the tail is less than 0.78×10^{-3} m, the undercooling gradually approaches the mean undercooling 33.6 K,

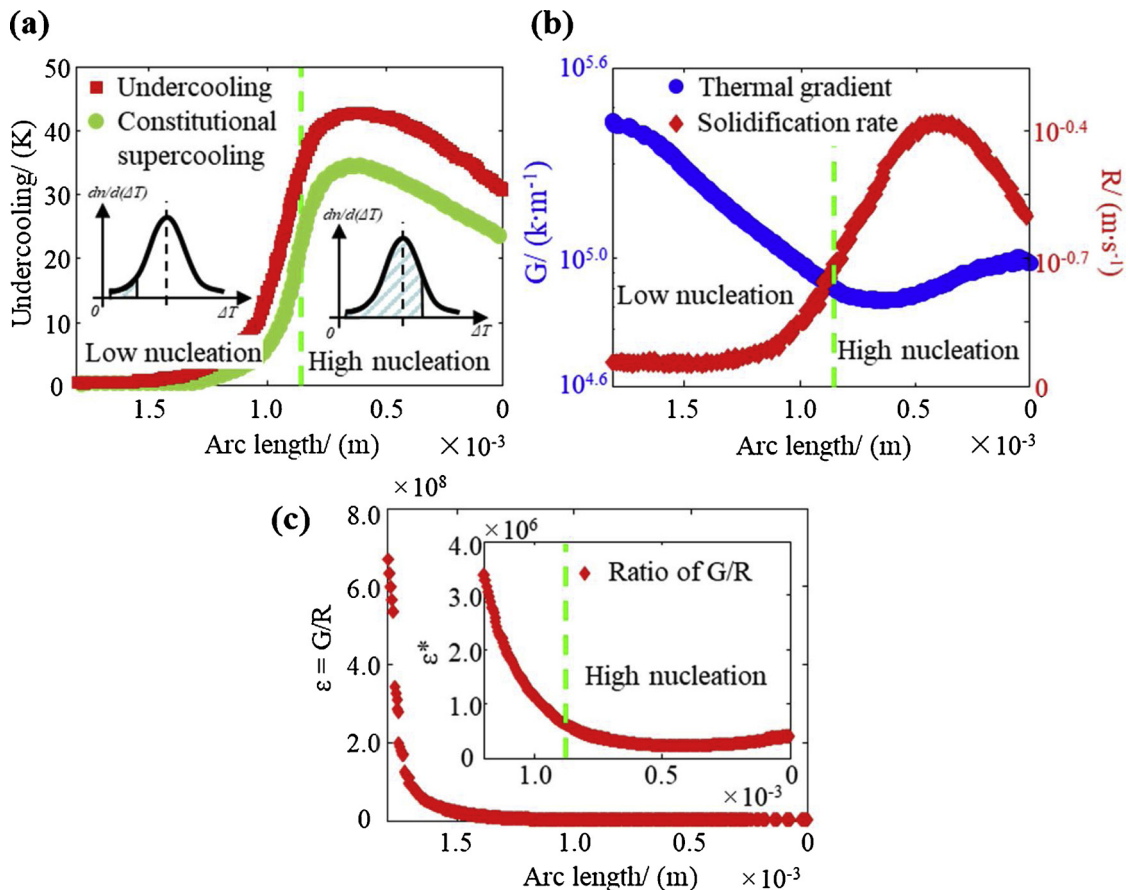


Fig. 4. (a) Shows the undercooling and constitutional supercooling along the arc length. The area under the Gaussian distribution is the probability of heterogeneous nucleation, (b) shows the thermal gradient and solidification rate along arc length, (c) presents the ratio of G/R at the tail of the melt pool near the S/L interface.

and even reach 43.0 K. According to the probability analysis based on Eq. (7), when the undercooling is larger than 33.6 K, the probability of heterogeneous nucleation exceeds 50.0% and up to 97.0% that can be considered as a high nucleation zone, as illustrated in the inset in Fig. 4a again. Such a high probability of the heterogeneous nucleation finally contributes to equiaxed grain growth near the tail of the melt pool. This well explains why equiaxed grains form near the centerline of the melt pool, as shown in Fig. 3a.

The CET of grain structures can further be interpreted by the thermal gradient, G , and solidification rate, R , as plotted in Fig. 4b. The effect of G is easily understood from Fig. 1c and the constitutional supercooling in the mushy zone decreases as G increase. In addition, the large R is expected to cause the high solute concentration gradient, which, in turn, increases the liquidus temperature gradient in the liquid, thus leading to the high constitutional supercooling. A ratio of $\epsilon = G/R$ is usually used to quantitatively evaluate their combined effect on the undercooling. The G is relatively large near the bottom of the melt pool ($10^{5.6} \sim 10^5 \text{ K}\cdot\text{m}^{-1}$), while the R is kept at a low value of about $1.0 \times 10^{-1.5} \text{ m}\cdot\text{s}^{-1}$. Thus, the relatively large ratio ϵ ($7.1 \times 10^8 \sim 2.2 \times 10^7 \text{ K}\cdot\text{s}\cdot\text{m}^{-2}$) is presented at the bottom as plotted in Fig. 4c. Based on the analyses above, such a large ϵ results in a small undercooling that subsequently suppresses the heterogeneous nucleation at this region. When approaching to the top of the melt pool, the lowered G and the enhanced R cause a decrease in ϵ accordingly, with a value about $3.1 \times 10^5 \text{ K}\cdot\text{s}\cdot\text{m}^{-2}$. Such a relatively small ϵ makes the undercooling increase, even up to 43.0 K, thus contributing to a high probability of nucleation.

The grain orientations of new nuclei are selected randomly, as shown in Fig. 3a, thus leading to a random texture in the equiaxed grains. On the other hand, competitive growth of grains with different orientations occurs during the epitaxial grain growth. The grains closely aligned with the maximum thermal gradient direction, *i.e.*, the N_z -direction, are found to dominate the epitaxial grain growth due to the grain selection. Here, only a single layer is simulated for the mechanism demonstration, and the similar grain growth processes take place during the printing of subsequent layers.

Fig. 5 exhibits the numerical and experimental [13] grain morphologies in the melt pool during In718 AM with the spot melting

pattern. Clearly, the spot melting strategy produces the fine equiaxed grains with random orientations, which agree closely with the experimental observations made by Raghavan et al. [13]. The formation of the fine equiaxed morphology is rationalized by the thermal information, *i.e.*, the undercooling that controls the heterogeneous nucleation in the melt pool, see Fig. 5c.

Fig. 6a presents the quantitative data about the undercooling, including constitutional supercooling, thermal and curvature undercoolings. It is readily observed the undercooling is comparably large with a minimum value around 40.5 K, which is larger than the mean undercooling ΔT_N of 33.6 K for IN718. Consequently, the probability of the heterogeneous nucleation is certainly high ($\geq 91.6\%$) that contributes to the fine equiaxed grain growth during rapid solidification. Further, it can be seen that the thermal gradient is low in the range of $10^{3.8} \sim 10^{4.0} \text{ K}\cdot\text{m}^{-1}$, and the solidification rate shows little change and stays around $10^{-1.6} \text{ m}\cdot\text{s}^{-1}$, as described in Fig. 6b. The reason for the low thermal gradient possibly is the natural preheating by the adjacent spots, before the heat source jumps to this spot for the melting. Such a low G then gives rise to a small ratio ϵ , with a maximum value of $4.6 \times 10^5 \text{ K}\cdot\text{s}\cdot\text{m}^{-2}$, see Fig. 6c, that makes the undercooling much larger than the mean undercooling ΔT_N .

4.2. $G - R$ map of solidified grain structures

Fig. 7a shows the G Vs R plot on a map of solidified grain structures for IN718 [7,14]. The simulation results, red circles (spot melting) and cruciate dots (line melting), are obtained under different preheating temperatures and scanning speeds. For purpose of comparison, the experimental results with cyan triangle and black pentagram are plotted in Fig. 7a for spot [13,14] and line melting [14,47,48], respectively. To systematically demonstrate the CET of grain structures in the melt pool, the representative results are presented in Fig. 7b–d for the spot melting, and Fig. 7e and f for the line melting with different building conditions.

It can be clearly seen that grains in the upper-left region are columnar, while the grains in the right-lower region are almost equiaxed. Increasing scanning speed (see the yellow arrow) and rising preheating temperature (see the green arrow) can reduce the temperature gradient

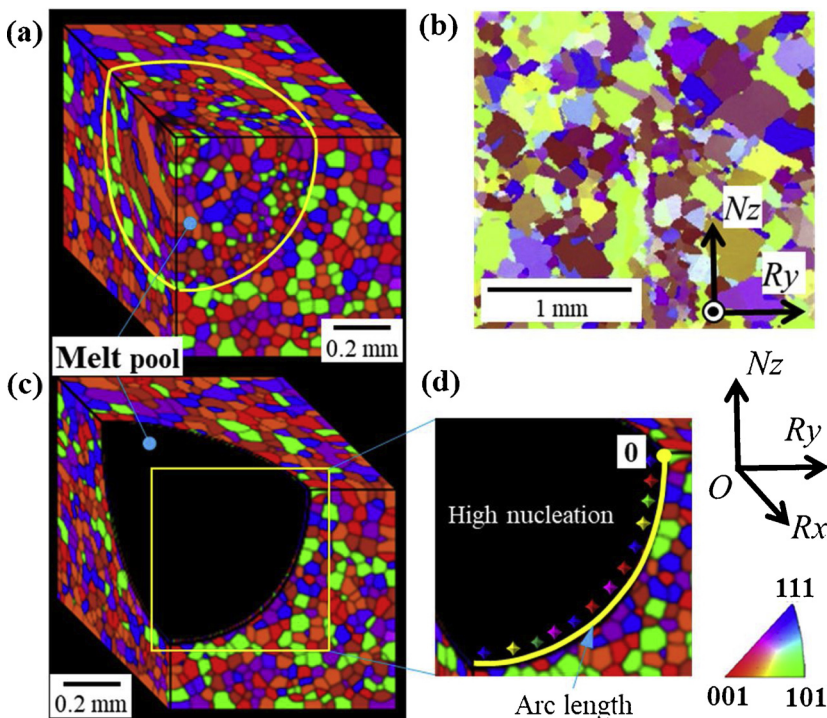


Fig. 5. Results of the spot melting strategy, (a) and (b) numerical and experimental [13] grain morphologies in the melt pool, (c) schematic of the high nucleation zones. The yellow line shows the arc length from the top to bottom of the melt pool (For interpretation of the references to colour in this figure legend, the reader is referred to the web version of this article).

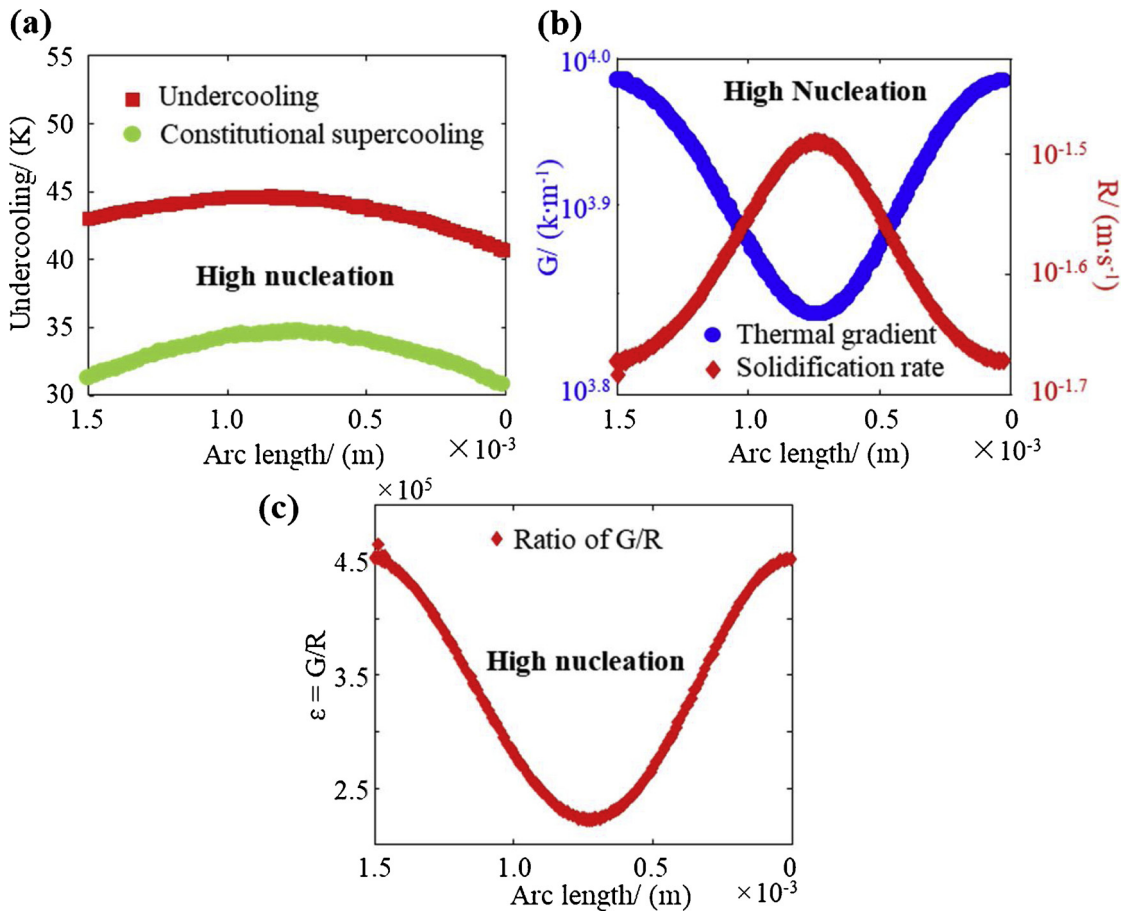


Fig. 6. (a) Shows the undercooling and constitutional supercooling along the arc length, (b) shows the thermal gradient and solidification rate along arc length, (c) presents the ratio of G/R near the S/L interface.

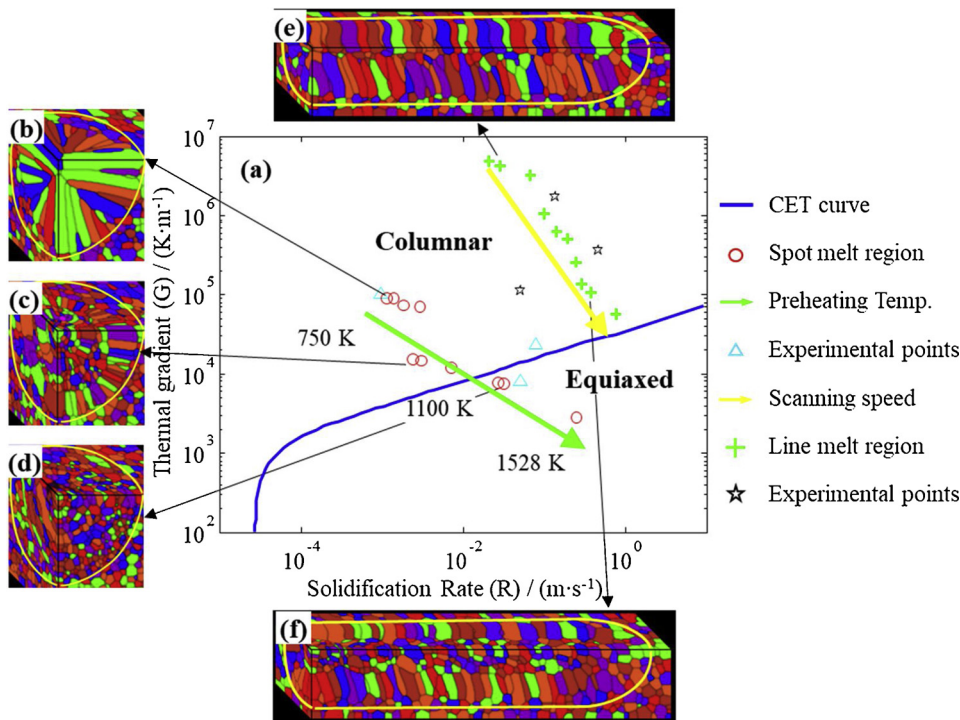


Fig. 7. The temperature gradient, G , Vs solidification rate, R , plot on a solidification map [7,14] of IN718. The simulation results, red circles (spot melting) and cruciate dots (line melting), are obtained under different preheating temperatures and scanning speeds. The experimental results are shown with cyan triangle and black pentagram for spot [13,14] and line melting [14,47,48], (b) - (d) show the representative grain morphologies in the melt pool for the spot melting strategy under variational preheating temperatures, similarly, the representative grain morphologies in the melt pool for the line melting strategy with increasing scanning speeds are shown in (e) and (f) (For interpretation of the references to colour in this figure legend, the reader is referred to the web version of this article).

and increase the solidification rate, so as to move the G - R map from the columnar towards the equiaxed grain patterns. Specified to the line melting strategy, with the increase of scanning speed from 0.02 to 0.8 $\text{m}\cdot\text{s}^{-1}$, the thermal gradient decreases from 8.0×10^6 to 6.0×10^4 $\text{K}\cdot\text{m}^{-1}$. As a result, the columnar grain structures (see Fig. 7e) gradually turn into the CET of grain structures (see Fig. 7f). Note that, it is difficult to fabricate the fully equiaxed grain structures by simply improving scanning speed, in which case other physical issues may arise, such as lack-of-fusion porosity, keyholing porosity and increased surface roughness [49–52].

The spot melting pattern provides a promising approach to manufacture the CET of grain structures, even for the fully equiaxed grain structures owing to the low thermal gradient (even $< 10^4$ $\text{K}\cdot\text{m}^{-1}$). The major reason lies in the preheating of adjacent spots before the electron beam jumps to one specific spot. If we increase the preheating temperature simultaneously, such a combined effect even more reduces the thermal gradient. For example, when the preheating temperature is set as a high value of 1528.0 K, and the electron beam power and spot on time are 1.2 KW and 1.0 ms, respectively, the thermal gradient even drops down to 3.0×10^3 $\text{K}\cdot\text{m}^{-1}$. This small thermal gradient produces a large undercooling and a high probability of heterogeneous nucleation that preferably form the fine equiaxed grain structures, as shown in Fig. 7d.

5. Conclusion

In summary, by using the well-tested multiscale PFM, we have uncovered how the CET of grain structures is formed during metallic AM. Using IN 718 as an example that is built by two strategies of spot and line melting, we demonstrate the CET of AM metals is critically controlled by the undercooling, mostly contributed by the constitutional supercooling in the melt pool, which dictates the extent of heterogeneous nucleation with respect to the grain epitaxial growth during rapid solidification. Increasing scanning speed and/or rising preheating temperature are found to reduce the temperature gradient and increase the solidification rate, thus leading to the large undercooling with a high probability of heterogeneous nucleation that contributes to the CET of grain structures. In particular, we found the spot melting presents a very low thermal gradient ($< 10^4$ $\text{K}\cdot\text{m}^{-1}$) due to the preheating effect from the local reheating of adjacent spots, thus making it as a promising way to achieve the fine equiaxed grain structures.

Acknowledgements

This work is financially supported by National Science Foundation of China (11872177), the Foundation for Innovative Research Groups of the National Natural Science Foundation of China (51621004), National Key R&D Program of China (2017YFB1002700), Science Fund of State Key Laboratory of Advanced Design and Manufacturing for Vehicle Body (71575003), Hunan Provincial Innovation Project of Graduate Student (CX2017B081) and the China Scholarship Council. Z. Wang, Y.H. Xiao, L. Chen are grateful for the financial support by the program of ORAU Ralph E. Powe Junior Faculty Enhancement Award and NSF CMMI, United States (1662854). The computer simulations were carried out on the clusters of High Performance Computing Collaboratory (HPC²) at Mississippi State University.

Appendix A. Supplementary data

Supplementary material related to this article can be found, in the online version, at doi:<https://doi.org/10.1016/j.addma.2018.12.019>.

References

- [1] P.L. Blackwell, The mechanical and microstructural characteristics of laser-deposited IN718, *J. Mater. Process. Technol.* 170 (2005) 240–246, <https://doi.org/10.1016/j.jmatprotec.2005.05.005>.
- [2] G.P. Dinda, A.K. Dasgupta, J. Mazumder, Texture control during laser deposition of nickel-based superalloy, *Scr. Mater.* 67 (2012) 503–506, <https://doi.org/10.1016/j.scriptamat.2012.06.014>.
- [3] J. Akram, P. Chalavadi, D. Pal, B. Stucker, Understanding grain evolution in additive manufacturing through modeling, *Addit. Manuf.* 21 (2018) 255–268, <https://doi.org/10.1016/j.addma.2018.03.021>.
- [4] X. Wang, K. Chou, Effects of thermal cycles on the microstructure evolution of Inconel 718 during selective laser melting process, *Addit. Manuf.* 18 (2017) 1–14, <https://doi.org/10.1016/j.addma.2017.08.016>.
- [5] J.H. Martin, B.D. Yahata, J.M. Hundley, J.A. Mayer, T.A. Schaedler, T.M. Pollock, 3D printing of high-strength aluminium alloys, *Nature* 549 (2017) 365–369, <https://doi.org/10.1038/nature23894>.
- [6] N. Raghavan, S. Simunovic, R. Dehoff, A. Plotkowski, J. Turner, M. Kirka, S. Babu, Localized melt-scan strategy for site specific control of grain size and primary dendrite arm spacing in electron beam additive manufacturing, *Acta Mater.* 140 (2017) 375–387, <https://doi.org/10.1016/j.actamat.2017.08.038>.
- [7] A. Plotkowski, M.M. Kirka, S.S. Babu, Verification and validation of a rapid heat transfer calculation methodology for transient melt pool solidification conditions in powder bed metal additive manufacturing, *Addit. Manuf.* 18 (2017) 256–268, <https://doi.org/10.1016/j.addma.2017.10.017>.
- [8] A.T. Sutton, C.S. Kriewall, M.C. Leu, J.W. Newkirk, A.T. Sutton, C.S. Kriewall, M.C. Leu, J.W. Newkirk, Powder characterization techniques and effects of powder characteristics on part properties in powder-bed fusion processes, *Virtual Phys. Prototyp.* 12 (2016) 3–29, <https://doi.org/10.1080/17452759.2016.1250605>.
- [9] S.L. Sing, F.E. Wiria, W.Y. Yeong, Selective laser melting of lattice structures: a statistical approach to manufacturability and mechanical behavior, *Robot. Comput. Integr. Manuf.* 49 (2018) 170–180, <https://doi.org/10.1016/j.rcim.2017.06.006>.
- [10] S. Price, B. Cheng, J. Lydon, K. Cooper, K. Chou, On process temperature in powder-bed electron beam additive manufacturing: process parameter effects, *J. Manuf. Sci. Eng.* 136 (2014) 61019, <https://doi.org/10.1115/1.4028485>.
- [11] B. Cheng, S. Shrestha, K. Chou, Stress and deformation evaluations of scanning strategy effect in selective laser melting, *Addit. Manuf.* 12 (2016) 240–251, <https://doi.org/10.1016/j.addma.2016.05.007>.
- [12] L.L. Parimi, G. Ravi, D. Clark, M.M. Attallah, Microstructural and texture development in direct laser fabricated IN718, *Mater. Charact.* 89 (2014) 102–111, <https://doi.org/10.1016/j.matchar.2013.12.012>.
- [13] N. Raghavan, R. Dehoff, S. Pannala, S. Simunovic, M. Kirka, J. Turner, N. Carlson, S.S. Babu, Numerical modeling of heat-transfer and the influence of process parameters on tailoring the grain morphology of IN718 in electron beam additive manufacturing, *Acta Mater.* 112 (2016) 303–314, <https://doi.org/10.1016/j.actamat.2016.03.063>.
- [14] J. Rapple, A. Plotkowski, M.M. Kirka, R. Dinwiddie, A. Okello, R.R. Dehoff, S.S. Babu, Thermographic microstructure monitoring in electron beam additive manufacturing, *Sci. Rep.* 7 (2017), <https://doi.org/10.1038/srep43554>.
- [15] L.E. Loh, C.K. Chua, W.Y. Yeong, J. Song, M. Mappar, S.L. Sing, Z.H. Liu, D.Q. Zhang, Numerical investigation and an effective modelling on the Selective Laser Melting (SLM) process with aluminium alloy 6061, *Int. J. Heat Mass Transf.* 80 (2015) 288–300, <https://doi.org/10.1016/j.ijheatmasstransfer.2014.09.014>.
- [16] A. Foroozmehr, M. Badrossamay, E. Foroozmehr, S. Golabi, Finite element simulation of selective laser melting process considering optical penetration depth of laser in powder bed, *Mater. Des.* 89 (2016) 255–263, <https://doi.org/10.1016/j.matdes.2015.10.002>.
- [17] P. Liu, X. Cui, J. Deng, S. Li, Z. Li, L. Chen, Investigation of thermal responses during metallic additive manufacturing using a “Tri-Prism” finite element method, *Int. J. Therm. Sci.* 136 (2019) 217–229, <https://doi.org/10.1016/j.ijthermalsci.2018.10.022>.
- [18] Y. Pei, X. Cui, A novel triangular prism element based on smoothed finite element method, *Int. J. Comput. Methods.* (2017), <https://doi.org/10.1142/S0219876218500585>.
- [19] S. Li, X. Cui, G. Li, Modelling and demonstration of electromagnetically assisted stamping system using an interactive mapping method, *Int. J. Mech. Sci.* 144 (2018) 312–323, <https://doi.org/10.1016/j.jimecs.2018.06.003>.
- [20] X. Cui, S. Li, H. Feng, G. Li, A triangular prism solid and shell interactive mapping element for electromagnetic sheet metal forming process, *J. Comput. Phys.* 336 (2017) 192–211, <https://doi.org/10.1016/j.jcp.2017.02.014>.
- [21] C.E. Krill III, L.-Q. Chen, Computer simulation of 3-D grain growth using a phase-field model, *Acta Mater.* 50 (2002) 3059–3075, [https://doi.org/10.1016/S1359-6454\(02\)00084-8](https://doi.org/10.1016/S1359-6454(02)00084-8).
- [22] L.-Q. Chen, Phase-field models for microstructure evolution, *Annu. Rev. Mater. Res.* 32 (2002) 113–140, <https://doi.org/10.1146/annurev.matsci.32.112001.132041>.
- [23] X. Wang, P.W. Liu, Y. Ji, Y. Liu, M.H. Horstemeyer, L. Chen, Investigation on microsegregation of IN718 alloy during additive manufacturing via integrated phase-field and finite-element modeling, *J. Mater. Eng. Perform.* (2018) 1–9, <https://doi.org/10.1007/s11665-018-3620-3>.
- [24] F. Yu, Y. Wei, Y. Ji, L.Q. Chen, Phase field modeling of solidification microstructure evolution during welding, *J. Mater. Process. Technol.* 255 (2018) 285–293, <https://doi.org/10.1016/j.jmatprotec.2017.12.007>.
- [25] L. Chen, H.W. Zhang, L.Y. Liang, Z. Liu, Y. Qi, P. Lu, J. Chen, L.Q. Chen, Modulation of dendritic patterns during electrodeposition: a nonlinear phase-field model, *J. Power Sources* 300 (2015) 376–385, <https://doi.org/10.1016/j.jpowsour.2015.09.055>.
- [26] X. Wang, B. Wang, M. Meyerson, C.B. Mullins, Y. Fu, L. Zhu, L. Chen, A phase-field model integrating reaction-diffusion kinetics and elasto-plastic deformation with application to lithiated selenium-doped germanium electrodes, *Int. J. Mech. Sci.* 144 (2018) 158–171, <https://doi.org/10.1016/j.jimecs.2018.05.040>.

- [27] H.H. Yan, Y.H. Bie, X.Y. Cui, G.P. Xiong, L. Chen, A computational investigation of thermal effect on lithium dendrite growth, *Energy Convers. Manag.* 161 (2018) 193–204, <https://doi.org/10.1016/j.enconman.2018.02.002>.
- [28] L. Chen, F. Fan, L. Hong, J. Chen, Y.Z. Ji, S.L. Zhang, T. Zhu, L.Q. Chen, A phase-field model coupled with large elasto-plastic deformation: application to lithiated silicon electrodes, *J. Electrochem. Soc.* 161 (2014) F3164–F3172, <https://doi.org/10.1149/2.0171411jes>.
- [29] Y. Ji, L. Chen, L.-Q. Chen, Understanding microstructure evolution during additive manufacturing of metallic alloys using phase-field modeling, thermo-mechanical model, *Addit. Manuf.* (2018) 93–116, <https://doi.org/10.1016/B978-0-12-811820-7.00008-2>.
- [30] Y. Ji, T.W. Heo, F. Zhang, L.Q. Chen, Theoretical assessment on the phase transformation kinetic pathways of multi-component Ti alloys: application to Ti-6Al-4V, *J. Phase Equilibria Diffus.* 37 (2016) 53–64, <https://doi.org/10.1007/s11669-015-0436-9>.
- [31] Y.Z. Ji, Z. Wang, B. Wang, Y. Chen, T. Zhang, L.Q. Chen, X. Song, L. Chen, Effect of meso-scale geometry on piezoelectric performances of additively manufactured flexible Polymer-Pb(Zr_xTi_{1-x})O₃Composites, *Adv. Eng. Mater.* 19 (2017), <https://doi.org/10.1002/adem.201600803>.
- [32] L. Chen, J. Chen, R.A. Lebensohn, Y.Z. Ji, T.W. Heo, S. Bhattacharyya, K. Chang, S. Mathaudhu, Z.K. Liu, L.Q. Chen, An integrated fast Fourier transform-based phase-field and crystal plasticity approach to model recrystallization of three dimensional polycrystals, *Comput. Methods Appl. Mech. Eng.* 285 (2015) 829–848, <https://doi.org/10.1016/j.cma.2014.12.007>.
- [33] P.W. Liu, Y.Z. Ji, Z. Wang, C.L. Qiu, A.A. Antonyamsy, L.Q. Chen, X.Y. Cui, L. Chen, Investigation on evolution mechanisms of site-specific grain structures during metal additive manufacturing, *J. Mater. Process. Technol.* 257 (2018) 191–202, <https://doi.org/10.1016/j.jmatprotec.2018.02.042>.
- [34] X. Wang, B. Wang, M. Meyerson, C.B. Mullins, Y. Fu, L. Zhu, A phase-field model integrating reaction-diffusion kinetics and elasto-plastic deformation with application to lithiated selenium-doped germanium electrodes, *Int. J. Mech. Sci.* (2018), <https://doi.org/10.1016/j.ijmecsci.2018.05.040>.
- [35] P. Schempp, C.E. Cross, A. Pittner, G. Oder, R.S. Neumann, H. Roosh, I. Dörfel, W. Österle, M. Rethmeier, Solidification of GTA aluminum weld metal: part 1 - grain morphology dependent upon alloy composition and grain refiner content, *Weld. J.* 93 (2014) 53s–59s <http://www.scopus.com/inward/record.url?eid=2-s2.0-84894495853&partnerID=40&md5=582808fb0841111a44f9c864754373a4>.
- [36] P. Schempp, C.E. Cross, A. Pittner, M. Rethmeier, Solidification of GTA aluminum weld metal: part 2 - thermal conditions and model for columnar-to-equiaxed transition, *Weld. J.* 93 (2014) 69s–77s <http://www.scopus.com/inward/record.url?eid=2-s2.0-84894423648&partnerID=40&md5=49c352be7db5504a5db3a7e43af5f03d>.
- [37] D. Shu, B. Sun, J. Mi, P.S. Grant, A quantitative study of solute diffusion field effects on heterogeneous nucleation and the grain size of alloys, *Acta Mater.* 59 (2011) 2135–2144, <https://doi.org/10.1016/j.actamat.2010.12.014>.
- [38] J. Zhang, F. Liou, W. Seufzer, K. Taminger, A coupled finite element cellular automaton model to predict thermal history and grain morphology of Ti-6Al-4V during direct metal deposition (DMD), *Addit. Manuf.* 11 (2016) 32–39, <https://doi.org/10.1016/j.addma.2016.04.004>.
- [39] C.A. Gandin, M. Rappaz, A coupled finite element-cellular automaton model for the prediction of dendritic grain structures in solidification processes, *Acta Metall. Mater.* 42 (1994) 2233–2246, [https://doi.org/10.1016/0956-7151\(94\)90302-6](https://doi.org/10.1016/0956-7151(94)90302-6).
- [40] J.N. DuPont, *Fundamentals of weld solidification*, ASM Int. (2011).
- [41] R. Trivedi, W. Kurz, Dendritic growth, *Int. Mater. Rev.* 39 (1994) 49–74, <https://doi.org/10.1179/imr.1994.39.2.49>.
- [42] D.H. StJohn, A. Prasad, M.A. Easton, M. Qian, The contribution of constitutional supercooling to nucleation and grain formation, *Metall. Mater. Trans. A Phys. Metall. Mater. Sci.* 46 (2015) 4868–4885, <https://doi.org/10.1007/s11661-015-2960-y>.
- [43] H. Search, C. Journals, A. Contact, M. Iopscience, M. Simul, I.P. Address, 3D probabilistic modelling of equiaxed eutectic solidification, *Model. Simul. Mater. Se. Eng.* 1 (1993) 455–466.
- [44] J. Kundin, L. Mushongera, H. Emmerich, Phase-field modeling of microstructure formation during rapid solidification in Inconel 718 superalloy, *Acta Mater.* 95 (2015) 343–356, <https://doi.org/10.1016/j.actamat.2015.05.052>.
- [45] S. Mohanty, J.H. Hattel, Laser additive manufacturing of multimaterial tool inserts: a simulation-based optimization study, *Laser 3D Manuf. IV, Int. Soc. Opt. Photon.* (2017) 100950G, <https://doi.org/10.1117/12.2253600>.
- [46] Z. Peng, F. Xie, J. Zhang, X. Wu, Effect of undercooling on microstructure evolution in IN718 superalloy, rare met, *Mater. Eng.* 42 (2013) 1988–1992, [https://doi.org/10.1016/S1875-5372\(14\)60012-6](https://doi.org/10.1016/S1875-5372(14)60012-6).
- [47] R.R. Dehoff, M.M. Kirka, W.J. Sames, H. Bilheux, A.S. Tremsin, L.E. Lowe, S.S. Babu, Site specific control of crystallographic grain orientation through electron beam additive manufacturing, *Mater. Sci. Technol.* 31 (2015) 931–938, <https://doi.org/10.1179/1743284714Y.0000000734>.
- [48] P. Promopattum, S.C. Yao, P.C. Pistorius, A.D. Rollett, A comprehensive comparison of the analytical and numerical prediction of the thermal history and solidification microstructure of inconel 718 products made by laser powder-bed fusion, *Engineering* 3 (2017) 685–694, <https://doi.org/10.1016/J.ENG.2017.05.023>.
- [49] C. Qiu, C. Panwisawas, M. Ward, H.C. Basoalto, J.W. Brooks, M.M. Attallah, On the role of melt flow into the surface structure and porosity development during selective laser melting, *Acta Mater.* 96 (2015) 72–79, <https://doi.org/10.1016/j.actamat.2015.06.004>.
- [50] M. Tang, P.C. Pistorius, J.L. Beuth, Prediction of lack-of-fusion porosity for powder bed fusion, *Addit. Manuf.* 14 (2017) 39–48, <https://doi.org/10.1016/j.addma.2016.12.001>.
- [51] Y. Tian, D. Tomus, P. Rometsch, X. Wu, Influences of processing parameters on surface roughness of Hastelloy X produced by selective laser melting, *Addit. Manuf.* 13 (2017) 103–112, <https://doi.org/10.1016/j.addma.2016.10.010>.
- [52] S.A. Fatemi, J.Z. Ashany, A.J. Aghchai, A. Abolghasemi, Experimental investigation of process parameters on layer thickness and density in direct metal laser sintering: a response surface methodology approach, *Virtual Phys. Prototyp.* 12 (2017) 133–140, <https://doi.org/10.1080/17452759.2017.1293274>.